

Unstructured Reynolds Stress Model Solutions for Turbulent Flow around a BELL 214ST Fuselage

Emre Alpman
 exa152@psu.edu
 Graduate Research Assistant

Lyle N. Long
 lnl@psu.edu
 Professor of Aerospace Engineering

Aerospace Engineering Department
 The Pennsylvania State University
 University Park, PA, 16802

ABSTRACT

Numerical simulation of high Reynolds number turbulent flow around a Bell 214ST helicopter fuselage is performed using an unstructured mesh. The computations include an application of Reynolds Stress Model (RSM), which consists of coupling the Reynolds transport equations with the Favre averaged Navier-Stokes Equations. The resulting system of 12 coupled, non-linear partial differential equations is solved using PUMA_RSM which is an in-house unstructured grid computational fluid dynamics code written in ANSI C++. In order to reduce the CPU time and memory requirements, parallel processing is applied with the MPI (Message Passing Interface) communication standard. Solutions are performed for an isolated fuselage at three different flow conditions and helicopter with rotors modeled using momentum theory in forward flight. Predicted pressure and drag force correlate well with the wind tunnel data and RSM is proved to be useful for turbulent flow around such a complex geometry.

NOTATION

C_p	specific heat at constant pressure	Re	freestream Reynolds number
$\overline{C_p}$	pressure coefficient	Re_T	turbulent Reynolds number
$(d_{ij})_n$	turbulent diffusion term for Reynolds stresses	S_{ij}	mean strain rate tensor
$(d_\epsilon)_n$	turbulent diffusion term for dissipation rate	\bar{t}_{ij}	mean viscous stress tensor
\tilde{E}	total energy per unit mass	T	main rotor thrust
$\overline{\overline{F}}$	convective flux tensor	T_{tr}	tail rotor thrust
$\overline{\overline{F_T}}$	turbulent flux tensor	$\tilde{u}, \tilde{v}, \tilde{w}$	mean velocity components
$\overline{\overline{F_v}}$	viscous flux tensor	x, y, z	Cartesian coordinates
\tilde{H}	total enthalpy per unit mass	y^+	non-dimensional distance
k	turbulent kinetic energy	α	flow angle of attack
\tilde{K}	laminar heat diffusion coefficient	δ_{ij}	Kronecker's delta
L	length of the fuselage	ϵ	turbulence dissipation rate
M	freestream Mach number	ϵ^*	modified turbulence dissipation rate
\mathbf{n}	surface pseudo-normals	ϵ_{ij}	turbulence dissipation tensor
\bar{p}	mean static pressure	$\bar{\mu}$	dynamic viscosity
P_{ij}	turbulence production tensor	μ_T	eddy viscosity
\mathbf{q}	conservative flow variable vector	$\bar{\nu}$	kinematic viscosity
\mathbf{Q}	turbulence source vector	$\bar{\rho}$	mean density
\bar{q}_i	laminar heat transfer rate	τ_{ij}	Reynolds stress tensor
\bar{q}_{Ti}	turbulent heat transfer rate	ϕ_{ij}	pressure redistribution term
		ψ	yaw angle

Presented at the American Helicopter Society 61st Annual Forum, Grapevine, TX, June 1 – 3, 2005.

Copyright © 2005 by the American Helicopter Society International, Inc. All rights reserved.

INTRODUCTION

The relatively complex and non-streamlined geometry of helicopter fuselages usually lead to separated flows. Separated flow around a body results in many phenomena in aerodynamics, such as drag increase, lift loss, unsteady fluctuations, etc. Therefore, accurate turbulence prediction is a key to understanding and predicting separated turbulent flows around aerodynamic devices¹. Figure 1 shows a general view of the turbulence models which are being used in the literature. It is evident from this figure that by using some assumptions and approximations, computationally cheaper models can be obtained but physics will be lost. The presence of three-dimensionality, vorticity and streamline curvature introduces changes in the turbulence structure, thus invalidating many of the turbulence models used widely for simple and mildly complex shear layers². Therefore, it becomes extremely important to employ more physics in providing suitable closure models for adequate prediction of these complex flows.

Many of the closure models in the literature (e.g. k- ϵ , k- ω , Spalart-Allmaras, Baldwin-Lomax) are eddy viscosity models, which are based on the Boussinesq approximation³ which assumes that the principal axes of the Reynolds stress tensor are coincident with those of the mean strain rate at all points in a turbulent flow. For complex three-dimensional flows with sudden changes in mean strain rate the Boussinesq hypothesis can be seriously in error because the Reynolds stresses will adjust to such changes at a rate unrelated to mean flow processes and time scales³. Figure 2 shows contours of turbulence time scale, (k/ϵ) normalized by the time scale of mean flow, $(1/S)$ where $S = \sqrt{S_{ij}S_{ij}}$ $S_{ij} = 0.5(\partial\tilde{u}_i/\partial x_j + \partial\tilde{u}_j/\partial x_i)$, at the center plane of the flow domain around the Bell 214ST fuselage at an angle of attack of 17.04 degrees. It is clear from this figure that in the regions when the quantity is much larger than one, the flow is distorted quite rapidly, which has a negative effect on the Boussinesq approximation. In addition to this, the concept of eddy viscosity is purely phenomenological and has no mathematical basis², and the isotropic nature of these models make them unsuitable for three-dimensional flows around complex geometries such as helicopter fuselages^{4,5}. While these models can be modified to improve their predictive accuracy, the modifications are largely ad hoc and cannot be easily generalized³. Moreover, in the case of strong separation, even the modified two-equation models were shown to fail to predict flow physics due to their isotropic nature⁶. Therefore, anisotropic models such as full Reynolds stress transport models (RSM)⁷ or Large Eddy Simulation (LES)⁸ are necessary for accurate prediction of three-dimensional separated flows. Although RSM does not represent the unsteady nature of turbulence as does dynamic models such as LES⁸, it is very effective in computing the time averaged quantities and is orders of magnitude cheaper than LES. In addition to this, uniform mesh requirement of LES lead to huge number of grid cells

in the vicinity of a solid boundary. To overcome this problem Detached Eddy Simulation (DES) can be considered as an alternative to LES. But in the near wall region DES uses the Boussinesq approximation, and it still is a dynamic method, hence expensive.

The present work employs RSM for simulation of turbulent flows around a Bell 214ST helicopter fuselage. The method consists of coupling the transport equations for Reynolds stresses and turbulence dissipation rate⁷ with the Favre-Reynolds averaged Navier-Stokes equations³ which results in a system of 12 coupled non-linear partial differential equations. The proposed model has been used and validated for various three-dimensional high Reynolds number flow computations using unstructured grids⁹. Figure 3 shows the vorticity contours at different axial stations along with the surface skin friction lines for turbulent flow around a 6:1 prolate spheroid from Ref. 9. This reference also contains comparisons for separated turbulent flow over a sphere. The asymptotic convergence of skin friction lines toward the primary and secondary separation lines were successfully observed and the locations of primary and secondary separation points were computed with an error of roughly three degrees. This clearly showed that the proposed RSM can handle three-dimensional separated flows where most of the eddy viscosity models would be insufficient. To the authors' knowledge, RSM has not been used before on a complex geometry such as a helicopter fuselage.

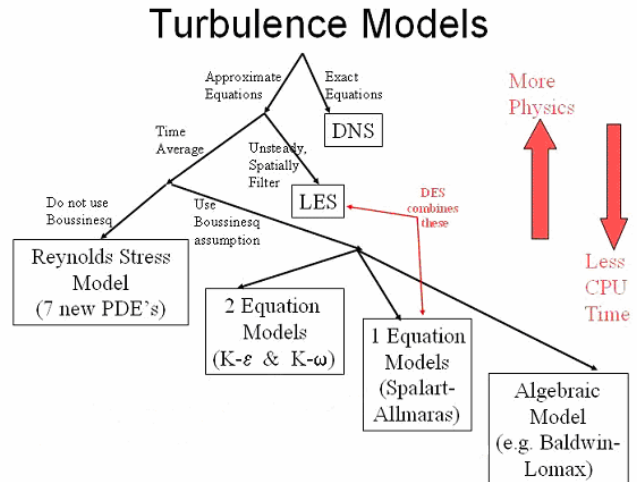


Figure 1 Turbulence Models

METHODOLOGY

The resulting system of 12 coupled non-linear partial differential equations is numerically solved using the computer code PUMA_RSM, which is an in-house computational fluid dynamics code written in ANSI C++. The equations are discretized by a second order finite volume method and solved using an explicit four-stage Runge-Kutta type integration technique. Although explicit

methods suffer from limitations on the maximum allowable time step size, they require a minimum number of arithmetic operations per iteration step and are easier to parallelize compared to implicit methods¹⁰.

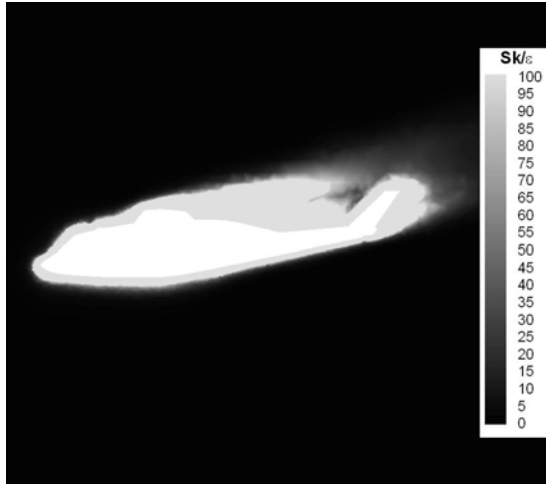


Figure 2 Contours of turbulent time scale normalized by mean flow time scale.
($Re = 1.5 \times 10^6$ per ft, $M = 0.2322$, $\alpha = 17.04$ degrees)

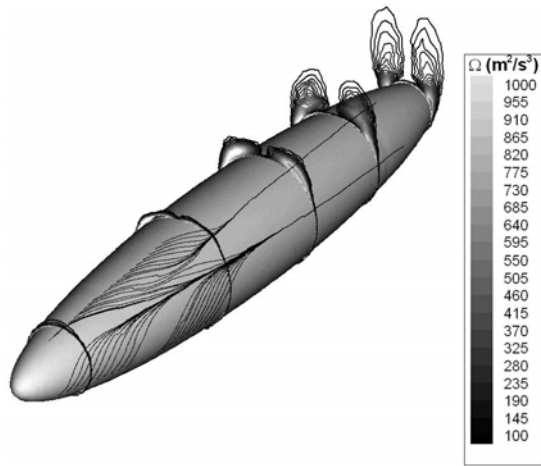


Figure 3 Vorticity contours at different axial locations with surface skin friction lines.
($Re = 6.5 \times 10^6$, $M = 0.1322$, $\alpha = 30$ degrees)

Solutions around a Bell 214ST fuselage are obtained using an unstructured mesh composed of 2.9 million tetrahedral cells. The y^+ values at the wall-adjacent cells were on the order of 40. Unstructured grids are relatively easy to construct around complex three-dimensional bodies and they offer very efficient cell distributions for accurate solutions of complex real life problems. The sectional views of the computational mesh generated for the problem are displayed in figures 4 and 5.

In order to include the rotors to the simulation, the main and tail rotors of the helicopter are modeled using actuator disks where a rotor is represented as a thin disk across which pressure undergoes a discontinuity while other variables remain continuous¹¹. The pressure jump across the disk can be computed using a momentum theory or a blade element theory. Blade element theory, being superior to momentum theory due to its more accurate model of the disk loads, is considered to be the best disk model and has been successfully employed for the predictions of steady and unsteady thrust response of the FANTAILTM of RAH66 Comanche helicopter in hover, forward flight and sideward flight¹²⁻¹⁵. But blade element theory requires the knowledge of blade and airfoil parameters. Without the knowledge of such parameters, momentum theory with a linear loading can be considered as a first approximation¹⁶.

In the present work, momentum theory with a linear load distribution is employed for the modeling of main and tail rotors. The main rotor thrust is equated to the maximum weight of the helicopter and tail rotor thrust is approximated using a simple momentum analysis¹¹.

In a computational sense, RSM costs much less than LES and Direct Numerical Simulation (DNS). The RSM equations have been time averaged, so they are not time dependent. LES and DNS are dynamic methods thus solutions require thousands or millions of time steps. RSM represents a 3-D problem, while LES and DNS are 4-D problems (space and time). But RSM still requires millions of grid cells and parallel processing is applied to reduce the CPU time and memory requirements. The MPI (Message Passing Interface)¹⁷ communication standard is used for this purpose and the code is run on a Beowulf cluster. The COSt Effective Computing Array (COCOAS3) is a cluster of off-the-shelf PCs connected via fast ethernet. These PCs run RedHat Linux with MPI¹⁷. COCOAS3 contains 60 2.4 GHz. dual Intel Xeon processors, each having 2 GB of RAM and dual 100 Mbps fast Ethernet cards.

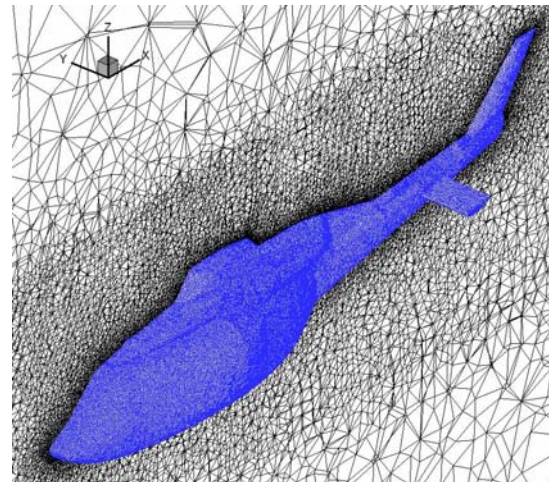


Figure 4 Sectional view of the computational mesh

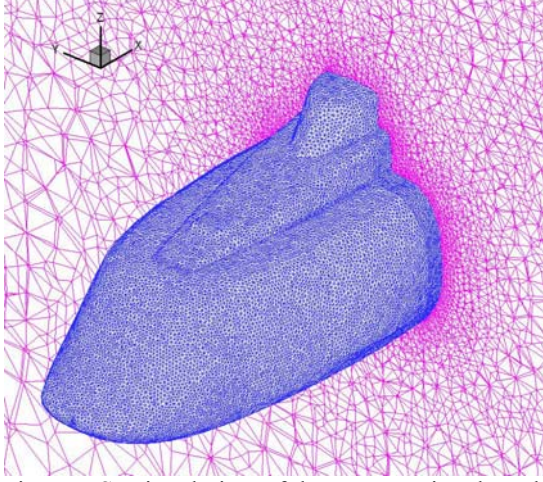


Figure 5 Sectional view of the computational mesh

MATHEMATICAL FORMULATION

The integral form of the governing equations (RSM) can be written as:

$$\frac{\partial}{\partial t} \int_{\Omega} \mathbf{q} d\Omega + \oint_S \bar{\bar{F}} \cdot d\mathbf{S} - \oint_S \bar{\bar{F}}_v \cdot d\mathbf{S} - \oint_S \bar{\bar{F}}_T \cdot d\mathbf{S} - \int_{\Omega} \mathbf{Q} d\Omega = 0 \quad (1)$$

where \mathbf{q} is the vector containing the conservative variables, $\bar{\bar{F}}$ is the convective flux tensor, $\bar{\bar{F}}_v$ is the viscous flux tensor, $\bar{\bar{F}}_T$ is the turbulent flux tensor and \mathbf{Q} is the vector containing turbulent source terms. The conservative variable vector \mathbf{q} can be written as:

$$\mathbf{q} = \left[\bar{\rho} \quad \bar{\rho} \tilde{u} \quad \bar{\rho} \tilde{v} \quad \bar{\rho} \tilde{w} \quad \bar{\rho} \tilde{E} \quad \dots \right. \\ \left. \dots \quad \tau_{xx} \quad \tau_{yy} \quad \tau_{zz} \quad \tau_{xy} \quad \tau_{xz} \quad \tau_{yz} \quad \bar{\rho} \varepsilon \right]^T \quad (2)$$

where $\bar{\rho}$ is the mean density, \tilde{u} , \tilde{v} , \tilde{w} are mean velocity components in the x , y and z -directions, \tilde{E} is the total energy per unit mass, τ_{ij} are the Reynolds stresses and ε is the turbulent dissipation rate. The details of the flux tensors and the source vector are as follows:

Convective Flux Tensor:

$$\bar{\bar{F}} = \begin{bmatrix} \bar{\rho} \tilde{u} & \bar{\rho} \tilde{v} & \bar{\rho} \tilde{w} \\ \bar{\rho} \tilde{u}^2 + \bar{p} & \bar{\rho} \tilde{u} \tilde{v} & \bar{\rho} \tilde{u} \tilde{w} \\ \bar{\rho} \tilde{u} \tilde{v} & \bar{\rho} \tilde{v}^2 + \bar{p} & \bar{\rho} \tilde{v} \tilde{w} \\ \bar{\rho} \tilde{u} \tilde{w} & \bar{\rho} \tilde{v} \tilde{w} & \bar{\rho} \tilde{w}^2 + \bar{p} \\ \bar{\rho} \tilde{u} \tilde{H} & \bar{\rho} \tilde{v} \tilde{H} & \bar{\rho} \tilde{w} \tilde{H} \\ \tilde{u} \tau_{xx} & \tilde{v} \tau_{xx} & \tilde{w} \tau_{xx} \\ \tilde{u} \tau_{yy} & \tilde{v} \tau_{yy} & \tilde{w} \tau_{yy} \\ \tilde{u} \tau_{zz} & \tilde{v} \tau_{zz} & \tilde{w} \tau_{zz} \\ \tilde{u} \tau_{xy} & \tilde{v} \tau_{xy} & \tilde{w} \tau_{xy} \\ \tilde{u} \tau_{xz} & \tilde{v} \tau_{xz} & \tilde{w} \tau_{xz} \\ \tilde{u} \tau_{yz} & \tilde{v} \tau_{yz} & \tilde{w} \tau_{yz} \\ \tilde{u} \tilde{\rho} \varepsilon & \tilde{v} \tilde{\rho} \varepsilon & \tilde{w} \tilde{\rho} \varepsilon \end{bmatrix} \quad (3)$$

where \tilde{H} is the total enthalpy per unit mass.

$$\tilde{H} = \tilde{E} + \frac{\bar{p}}{\bar{\rho}} \quad (4)$$

Viscous Flux Tensor:

$$\bar{\bar{F}}_v = \begin{bmatrix} 0 & 0 & 0 \\ \bar{t}_{xx} & \bar{t}_{xy} & \bar{t}_{xz} \\ \bar{t}_{xy} & \bar{t}_{yy} & \bar{t}_{yz} \\ \bar{t}_{xz} & \bar{t}_{yz} & \bar{t}_{zz} \\ \left(\begin{array}{c} \bar{t}_{xx} \tilde{u} + \bar{t}_{xy} \tilde{v} \\ + \bar{t}_{xz} \tilde{w} - \bar{q}_x \end{array} \right) & \left(\begin{array}{c} \bar{t}_{xy} \tilde{u} + \bar{t}_{yy} \tilde{v} \\ + \bar{t}_{yz} \tilde{w} - \bar{q}_y \end{array} \right) & \left(\begin{array}{c} \bar{t}_{xz} \tilde{u} + \bar{t}_{yz} \tilde{v} \\ + \bar{t}_{zz} \tilde{w} - \bar{q}_z \end{array} \right) \\ 0 & 0 & 0 \\ 0 & 0 & 0 \\ 0 & 0 & 0 \\ 0 & 0 & 0 \\ 0 & 0 & 0 \\ 0 & 0 & 0 \end{bmatrix} \quad (5)$$

where the mean viscous stresses and laminar heat transfer rates are approximated as follows¹⁸:

$$\bar{t}_{ij} \cong \bar{\mu} \left(\frac{\partial \tilde{u}_i}{\partial x_j} + \frac{\partial \tilde{u}_j}{\partial x_i} \right) - \frac{2}{3} \bar{\mu} \frac{\partial \tilde{u}_k}{\partial x_k} \delta_{ij} \quad (6)$$

$$\bar{q}_i \cong -\bar{K} \frac{\partial \bar{T}}{\partial x_i} \quad (7)$$

Turbulent Flux Tensor:

$$\overline{\overline{F}}_T = \begin{bmatrix} 0 & 0 & 0 \\ \tau_{xx} & \tau_{xy} & \tau_{xz} \\ \tau_{xy} & \tau_{yy} & \tau_{yz} \\ \tau_{xz} & \tau_{yz} & \tau_{zz} \\ \left(\begin{array}{l} \tau_{xx}\tilde{u} + \tau_{xy}\tilde{v} \\ + \tau_{xz}\tilde{w} - q_{Tx} \end{array} \right) & \left(\begin{array}{l} \tau_{xy}\tilde{u} + \tau_{yy}\tilde{v} \\ + \tau_{yz}\tilde{w} - q_{Ty} \end{array} \right) & \left(\begin{array}{l} \tau_{xz}\tilde{u} + \tau_{yz}\tilde{v} \\ + \tau_{zz}\tilde{w} - q_{Tz} \end{array} \right) \\ (d_{xx})_1 & (d_{xx})_2 & (d_{xx})_3 \\ (d_{yy})_1 & (d_{yy})_2 & (d_{yy})_3 \\ (d_{zz})_1 & (d_{zz})_2 & (d_{zz})_3 \\ (d_{xy})_1 & (d_{xy})_2 & (d_{xy})_3 \\ (d_{xz})_1 & (d_{xz})_2 & (d_{xz})_3 \\ (d_{yz})_1 & (d_{yz})_2 & (d_{yz})_3 \\ (d_\varepsilon)_1 & (d_\varepsilon)_2 & (d_\varepsilon)_3 \end{bmatrix} \quad (8)$$

where $(d_{ij})_n$ and $(d_\varepsilon)_n$ are diffusion terms for Reynolds stresses and turbulent dissipation term, respectively. Here the diffusion of Reynolds stresses is modeled using the triple correlations model of Daly and Harlow¹⁹.

$$(d_{ij})_n = -C_s \frac{k}{\varepsilon} \left[\tau_{nm} \frac{\partial \tau_{ij}}{\partial x_m} \right] + \tilde{\nu} \frac{\partial \tau_{ij}}{\partial x_n} \quad (9)$$

A similar expression is written for the turbulent dissipation rate:

$$(d_\varepsilon)_n = -C_\varepsilon \frac{k}{\varepsilon} \left[\tau_{nm} \frac{\partial \varepsilon}{\partial x_m} \right] + \tilde{\nu} \frac{\partial \varepsilon}{\partial x_n} \quad (10)$$

Where $C_s = 0.22$, $C_\varepsilon = 0.18$. In the above equations, k is the turbulent kinetic energy.

$$k = -\frac{1}{2\bar{\rho}}(\tau_{ii}) \quad (11)$$

The turbulent heat transfer rates are approximated using a simple gradient model²⁰.

$$\bar{q}_n \cong -\frac{\mu_T C_p}{Pr_T} \frac{\partial \bar{T}}{\partial x_n} \quad (12)$$

where²¹

$$\mu_T = C_\mu \tilde{\mu} Re_T \quad (13)$$

$$Re_T = \frac{\bar{\rho} k^2}{\tilde{\mu} \varepsilon}, \quad C_\mu = 0.09 \exp\left[\frac{-2.5}{(1+0.02 Re_T)}\right] \quad (14)$$

Turbulent Source Vector:

$$\mathbf{Q} = \begin{bmatrix} 0 \\ 0 \\ 0 \\ 0 \\ -P_{xx} + \bar{\rho}\varepsilon_{xx} - \phi_{xx} \\ -P_{yy} + \bar{\rho}\varepsilon_{yy} - \phi_{yy} \\ -P_{zz} + \bar{\rho}\varepsilon_{zz} - \phi_{zz} \\ -P_{xy} + \bar{\rho}\varepsilon_{xy} - \phi_{xy} \\ -P_{xz} + \bar{\rho}\varepsilon_{xz} - \phi_{xz} \\ -P_{yz} + \bar{\rho}\varepsilon_{yz} - \phi_{yz} \\ S \end{bmatrix} \quad (15)$$

where P_{ij} is the exact production term due to mean strain rates⁷:

$$P_{ij} = \tau_{ik} \frac{\partial \tilde{u}_j}{\partial x_k} + \tau_{jk} \frac{\partial \tilde{u}_i}{\partial x_k} \quad (16)$$

The dissipation tensor $\bar{\rho}\varepsilon_{ij}$ is approximated using local isotropy assumption³

$$\bar{\rho}\varepsilon_{ij} = \frac{2}{3}\bar{\rho}\varepsilon\delta_{ij} \quad (17)$$

The ϕ_{ij} term in Equation (15) is the pressure redistribution term. This term is the most important item in the closure because it controls both the separation and reattachment processes^{21,22-24}. The term is split into slow and rapid parts³ and their corresponding wall echo terms which arise from the reflection of pressure fluctuations from the rigid wall²⁵. The slow and the rapid terms are modeled as follows²⁶:

$$\phi_{ij,1} \cong -C_1 \bar{\rho} \varepsilon \left(-\frac{\tau_{ij}}{\bar{\rho}k} - \frac{2}{3}\delta_{ij} \right) \quad (18)$$

$$\phi_{ij,2} \cong -C_2 \left(P_{ij} - \frac{1}{3}P_{mm}\delta_{ij} \right) \quad (19)$$

The coefficients C_1 , C_2 are optimized by Launder and Shima²⁵. The models for slow²⁷ and rapid²⁶ wall echo terms are displayed in the following equations:

$$\phi_{ij,1}^w \cong -C_1^w \frac{\varepsilon}{k} \left[\tau_{km} n_k n_m \delta_{ij} - \frac{3}{2} \tau_{ki} n_k n_j - \frac{3}{2} \tau_{kj} n_k n_i \right] \quad (20)$$

$$\phi_{ij,2}^w \equiv C_2^w \left[\phi_{km,2} n_k n_m \delta_{ij} - \frac{3}{2} \phi_{ki,2} n_k n_j - \frac{3}{2} \phi_{kj,2} n_k n_i \right] \quad (21)$$

where \mathbf{n} is the surface pseudo-normal approximated by the gradient of a function of the turbulence length scale. The effect of distance from the wall is included in the coefficients C_1^w , C_2^w which are optimized by Gerolymos and Vallet²². Finally the source term S is given by the following relation³:

$$S = C_{\epsilon 1} \frac{\epsilon}{k} \tau_{ij} \frac{\partial \tilde{u}_i}{\partial x_j} - C_{\epsilon 2} \bar{\rho} \frac{\epsilon \epsilon^*}{k} \quad (22)$$

where ϵ^* is the modified dissipation rate which goes to zero at the solid wall²⁵.

NUMERICAL METHOD

The governing equations are numerically solved using an unstructured grid finite volume technique, which employs a modified Roe scheme²⁸ for convective fluxes and space centered scheme for viscous and turbulent fluxes. The resulting semi-discrete equations are numerically integrated using a four stage Runge-Kutta integration technique with local time stepping to enhance the convergence to steady state. The solution of the equations requires appropriate time steps limited by the stability bound of the scheme. The local time step is computed through stability analyses for the inviscid convection, viscous diffusion, turbulent diffusion and turbulent dissipation. At the solid boundaries a no slip condition is applied where all the velocity components, as well as the Reynolds stresses, are set to zero. The turbulent dissipation rate at the wall is computed using Equation (23)

$$\epsilon_w = 2\tilde{\nu} \left(\frac{\partial \sqrt{k}}{\partial n} \right)^2 \quad (23)$$

Where n is the normal direction to the wall. The solid boundaries are also assumed to be adiabatic.

RESULTS AND DISCUSSION

Results include high Reynolds number turbulent flow over an isolated Bell 214ST fuselage for three flight conditions and helicopter simulations with rotors modeled using linear momentum theory. The freestream Reynolds number and freestream Mach number are set to 1.5×10^6 per ft and 0.2322, respectively. The three isolated fuselage cases are low angle of attack cruise, high angle of attack, and high yaw angle. Helicopter simulations with rotors are performed only for low angle of attack cruise condition. Numerical

solutions are obtained after the L2 norm of the relative residual dropped four orders.

Low angle of attack cruise condition:

For this numerical solution the angle of attack is set to -2.28 degrees. Figure 6 shows the surface pressure distribution and Figure 7 shows the comparison of dorsal centerline pressure distribution with the experimental data²⁹. The predictions are in good agreement with the measurements.

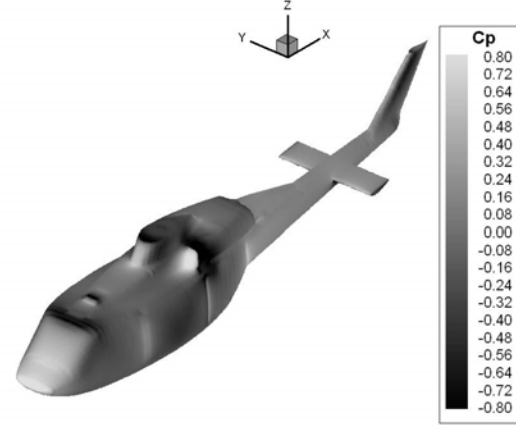


Figure 6 Surface pressure distribution
($\alpha = -2.28$ degrees, $\psi = 0$ degrees)

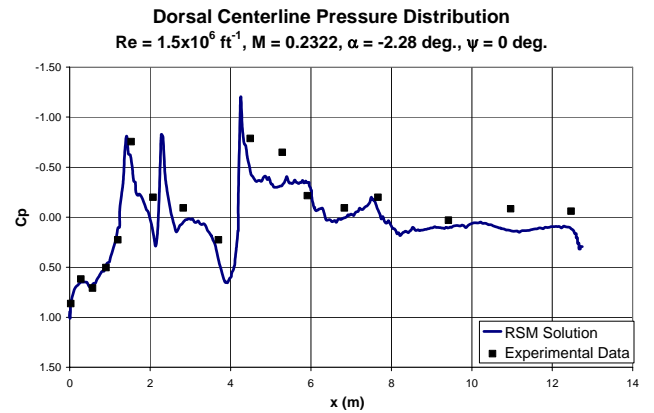


Figure 7 Comparison of computed dorsal centerline pressure distribution with experiment
($\alpha = -2.28$ degrees, $\psi = 0$ degrees)

In order to analyze the turbulent structure of the flow, normalized τ_{xz} and τ_{yz} distributions are plotted on the corresponding x - z and y - z planes, and displayed in Figures 8 and 9. Normalization is performed by dividing the quantity by mean density and turbulent kinetic energy. Isotropic turbulence is achieved when the diagonal terms of the Reynolds stress tensor are equal to each other and the off-diagonal terms are equal to zero. Thus in isotropic

turbulence normalized τ_{xz} and τ_{yz} become zero. The inhomogeneity and anisotropy of turbulence is evident from these figures where the contour quantities are non zero and change spatially.

High Angle of Attack Condition:

For this case the angle of attack is set to 17.4 degrees. Figure 10 shows the surface pressure distribution and Figure 11 shows the comparison of dorsal centerline pressure distribution with the experimental data²⁹. The predictions are in good agreement with the experiment. The expansion around the canopy region is much stronger than the previous case but PUMA_RSM gives good agreement even where the expansions are quite abrupt.

Normalized τ_{xz} and τ_{yz} distributions on the corresponding x - z and y - z planes are displayed in figures 12 and 13. The effect of flow angle of attack on the Reynolds stresses can be seen. In order to check the effectiveness of RSM, Reynolds stresses are recomputed using the Boussinesq approximation with an eddy viscosity computed using equations (13) and (14). Figure 14 shows the normalized τ_{xz} computed with this method and figure 15 shows the difference between the normalized τ_{xz} 's computed using the Boussinesq approximation and RSM. Comparison of figures 12 and 14, and analysis of figure 15 clearly shows that Reynolds stresses and mean strain rates are grossly misaligned. This suggests that turbulence models based on the Boussinesq approximation might perform poorly for this flow and warrants the use of RSM.

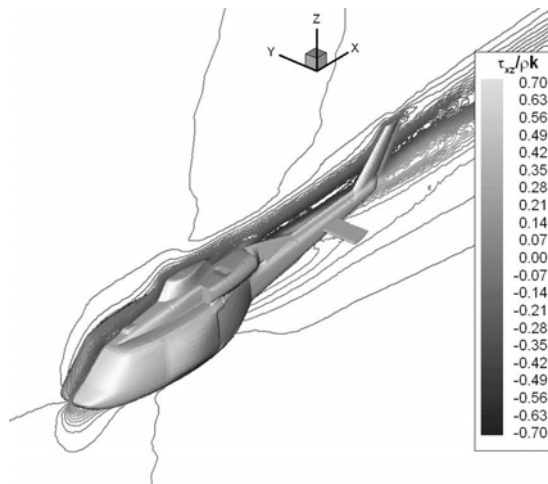


Figure 8 Normalized τ_{xz} contours ($\alpha = -2.28$ degrees, $\psi = 0$ degrees)

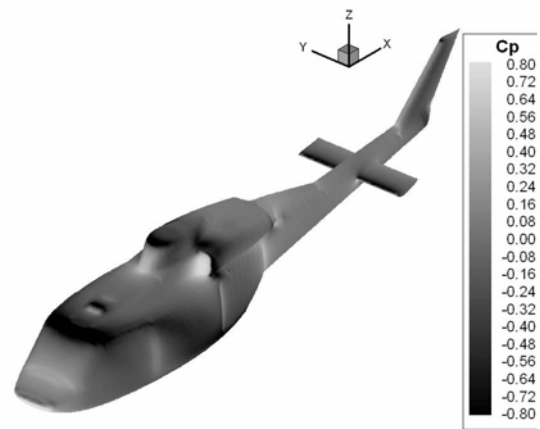


Figure 10 Surface pressure distribution ($\alpha = 17.04$ degrees, $\psi = 0$ degrees)

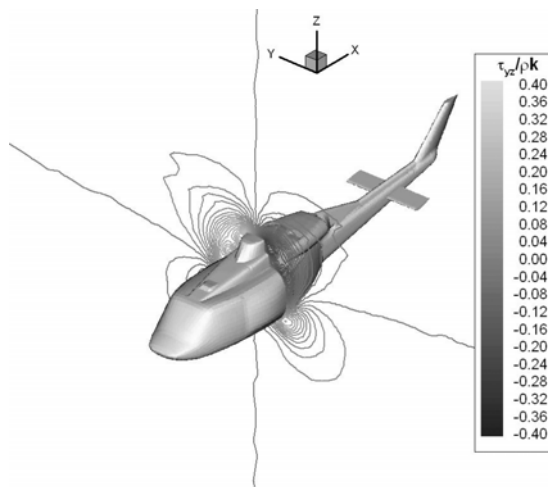


Figure 9 Normalized τ_{yz} contours ($\alpha = -2.28$ degrees, $\psi = 0$ degrees)

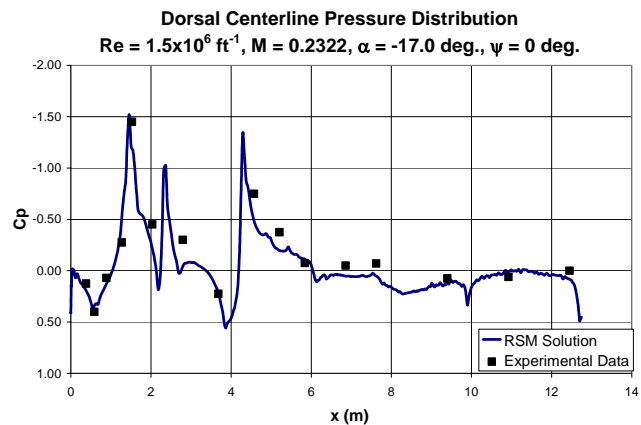


Figure 11 Comparison of computed dorsal centerline pressure distribution with experiment ($\alpha = 17.04$ degrees, $\psi = 0$ degrees)

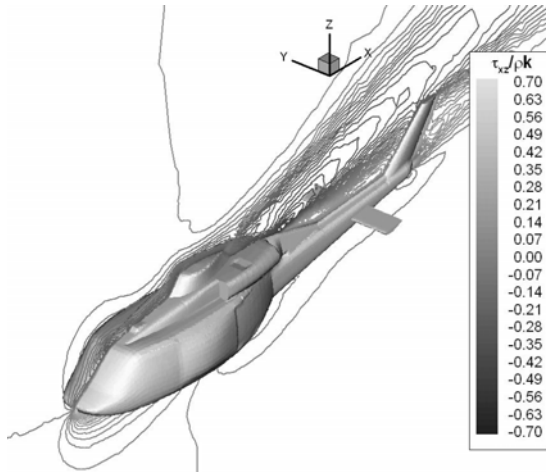


Figure 12 Normalized τ_{xz} contours ($\alpha = 17.04$ degrees, $\psi = 0$ degrees)

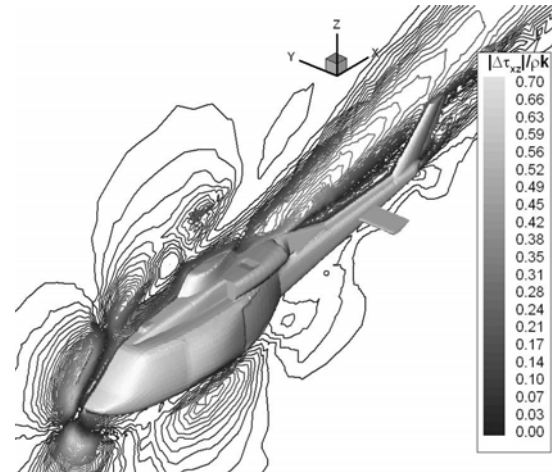


Figure 15 Difference between the normalized τ_{xz} contours computed using Boussinesq approximation and RSM. ($\alpha = 17.04$ degrees, $\psi = 0$ degrees)

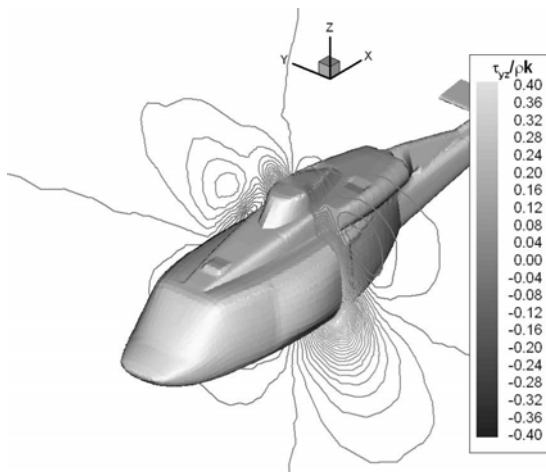


Figure 13 Normalized τ_{yz} contours ($\alpha = 17.04$ degrees, $\psi = 0$ degrees)

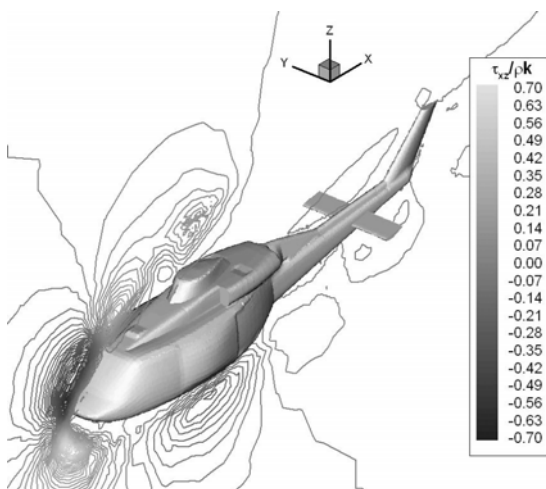


Figure 14 Normalized τ_{xz} contours computed using Boussinesq approximation ($\alpha = 17.04$ degrees, $\psi = 0$ degrees)

High Yaw Angle Condition:

For this case the yaw angle is set to 16.4 degrees and angle of attack is set to -1.6 degrees. Surface pressure distribution and comparison of dorsal centerline pressure distribution with the experimental data²⁹ are displayed in figures 16 and 17. A non-symmetric pressure distribution is especially evident on the elevator. Pressure predictions are in good agreement with experiment except in the tailboom region. Here the predicted pressure is higher than the measurements. Such a behavior was also observed in Navier-Stokes simulations by Narramore and Brand³⁰. The discrepancy in the tail boom region might be due to the crossflow coming through the engine exhaust which was not included in our computational simulation.

Normalized τ_{xz} and τ_{yz} distributions for this case are displayed in figures 18 and 19. Effect of side flow on the Reynolds stresses can be observed.

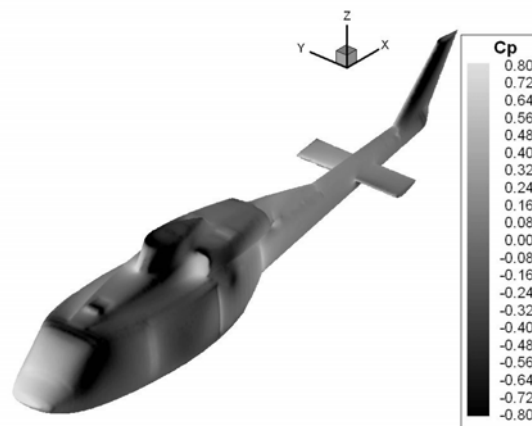


Figure 16 Surface pressure distribution ($\alpha = -1.6$ degrees, $\psi = 16.4$ degrees)

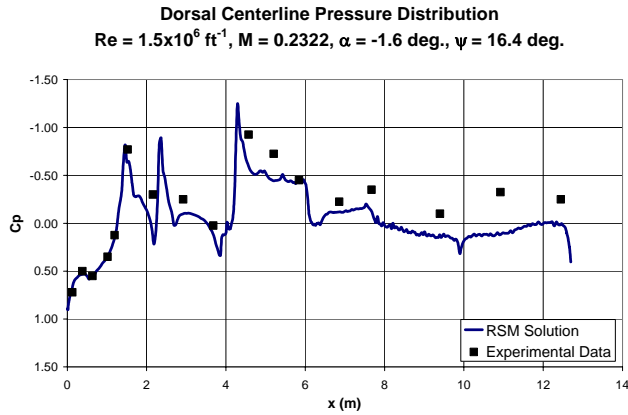


Figure 17 Comparison of computed dorsal centerline pressure distribution with experiment ($\alpha = -1.6$ degrees, $\psi = 16.4$ degrees)

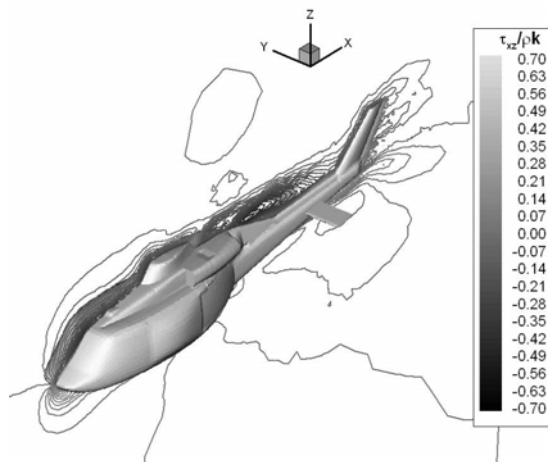


Figure 18 Normalized τ_{xz} contours ($\alpha = -1.6$ degrees, $\psi = 16.4$ degrees)

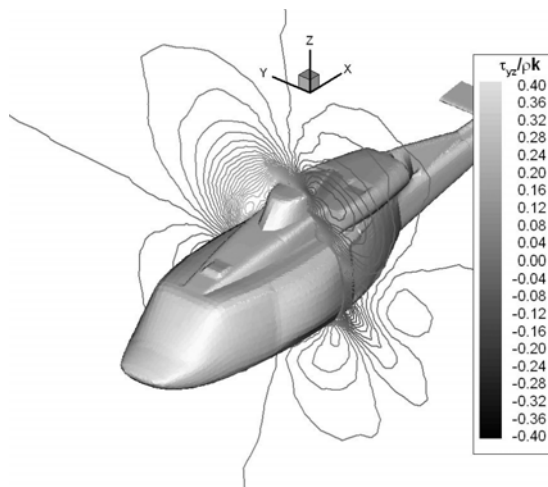


Figure 19 Normalized τ_{yz} contours ($\alpha = -1.6$ degrees, $\psi = 16.4$ degrees)

Helicopter Simulation with Rotors:

In this case main and tail rotors, modeled using momentum theory with linear load distribution, are included the low angle of attack cruise condition case. Here the main rotor thrust is taken as 17,500 lbs. and tail rotor thrust is approximated to be 1104 lbs after a simple trim analysis using momentum theory. In order to see the effect of the rotors on the flowfield, the pressure distributions at $x/L = 0.32$ and $x/L = 0.95$ are plotted with and without rotors in figures 20, 21, 22 and 23, respectively. The effect of the main rotor and also the tail rotor can be observed from these figures. The contours of normalized \tilde{w} velocity on the main rotor plane are shown in figure 24. For comparison purposes solution without the rotors is also included in figure 25.

The induced velocity due to pressure jump across the main rotor disk is observed in these figures. One can also see adjacent positive and negative \tilde{w} values in the vicinity of the rotor perimeter in Figure 24. This clearly implies the tip vortex formation. This vortical flowfield is then convected downstream. It is clear that the presence of the rotors not only induces additional flow gradients but also generates a vortical flowfield which travels downstream. This induced flow will change the turbulence structure. In order to analyze the effects of rotors, normalized τ_{xz} and τ_{yz} distributions are plotted in figures 26 and 27. Solutions without rotors were previously displayed in figures 8 and 9. Comparing figures 8 and 26 the effect of the main rotor on the turbulence structure can be observed. Here the effects are mainly due to additional flow gradients because tip vortices are weaker in this plane. The effects of tip vortices can be analyzed by comparing figures 9 and 27. It is evident that induced vortical flow increases the turbulence inhomogeneity and anisotropy. In order to see the effect of the tail rotor and the convecting tip vortices, the normalized τ_{yz} distributions are plotted at $x/L = 0.95$ with and without rotors in Figures 28 and 29. It is clear from these figures that tail rotor has a small effect on turbulence structure. But other than that one can easily observe some contours away from the helicopter in figure 28 which are not seen in figure 29. This shows the turbulence induced by the downstream traveling tip vortices.

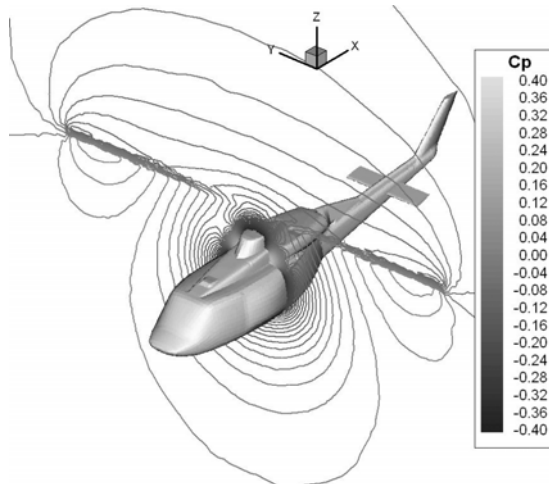


Figure 20 Pressure distribution at $x/L = 0.32$
 $(\alpha = -2.28$ degrees, $\psi = 0$ degrees)
 $(T = 17500$ lbs., $T_{tr} = 1104$ lbs.)

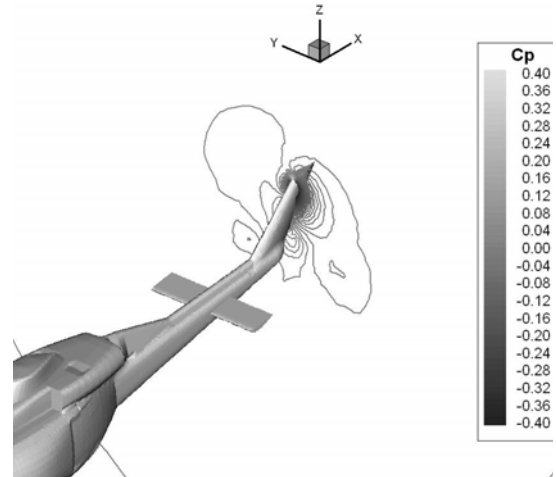


Figure 23 Pressure distribution $x/L = 0.95$
 $(\alpha = -2.28$ degrees, $\psi = 0$ degrees) (without rotors)

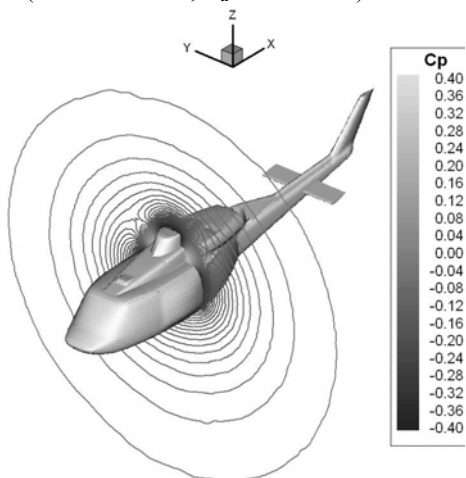


Figure 21 Pressure distribution $x/L = 0.32$
 $(\alpha = -2.28$ degrees, $\psi = 0$ degrees) (without rotors)

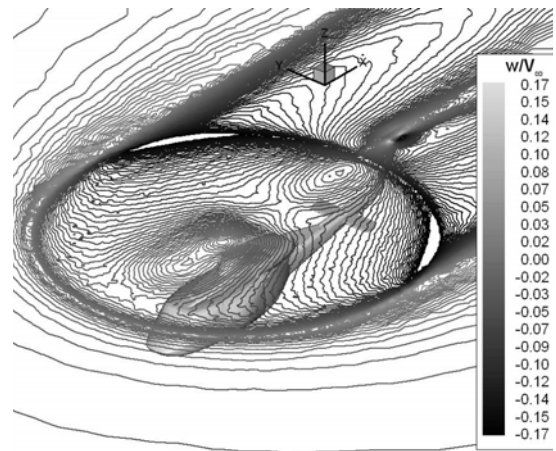


Figure 24 Normalized \tilde{w} distribution at the main rotor plane
 $(\alpha = -2.28$ degrees, $\psi = 0$ degrees)
 $(T = 17500$ lbs., $T_{tr} = 1104$ lbs)

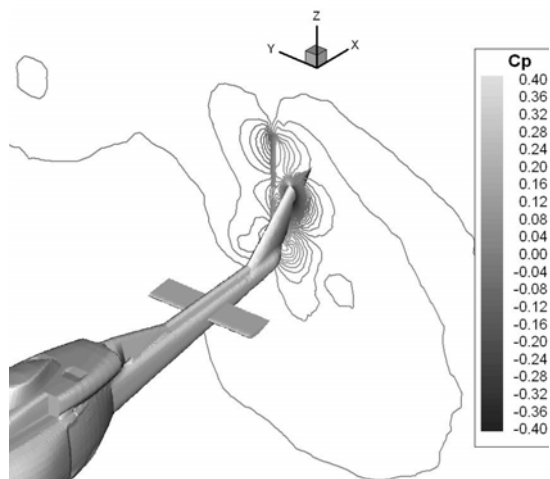


Figure 22 Pressure distribution at $x/L = 0.95$
 $(\alpha = -2.28$ degrees, $\psi = 0$ degrees)
 $(T = 17500$ lbs., $T_{tr} = 1104$ lbs.)

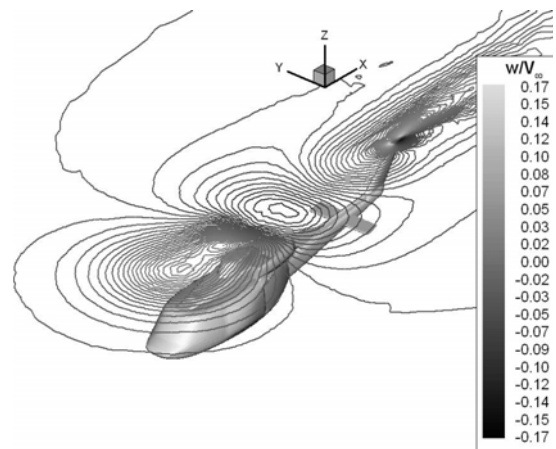


Figure 25 Normalized \tilde{w} distribution at the main rotor plane
 $(\alpha = -2.28$ degrees, $\psi = 0$ degrees) (without rotors)

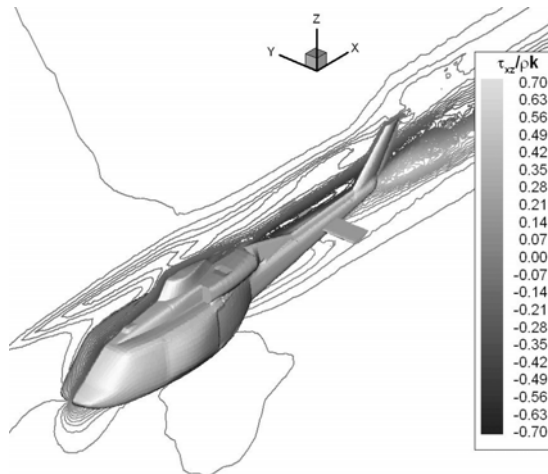


Figure 26 Normalized τ_{xz} contours
 $(\alpha = -2.28$ degrees, $\psi = 0$ degrees)
 $(T = 17500$ lbs., $T_{tr} = 1104$ lbs)

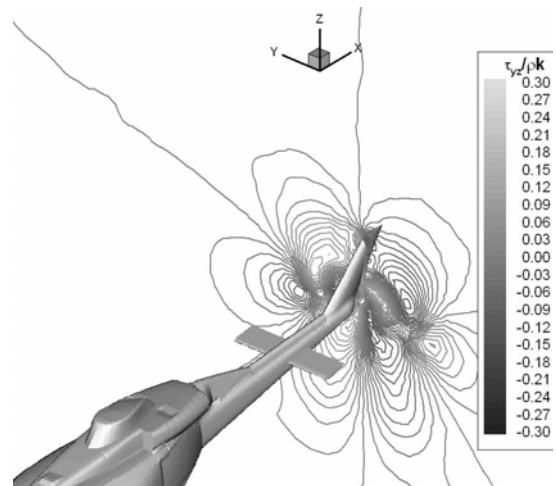


Figure 29 Normalized τ_{yz} contours at $x/L = 0.95$
 $(\alpha = -2.28$ degrees, $\psi = 0$ degrees) (without rotors)

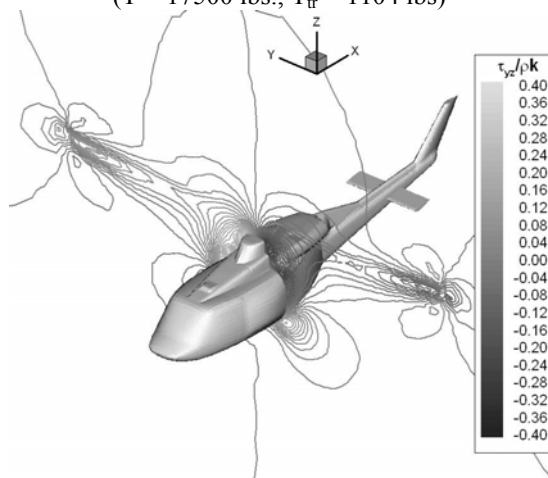


Figure 27 Normalized τ_{yz} contours at $x/L = 0.32$
 $(\alpha = -2.28$ degrees, $\psi = 0$ degrees)
 $(T = 17500$ lbs., $T_{tr} = 1104$ lbs)

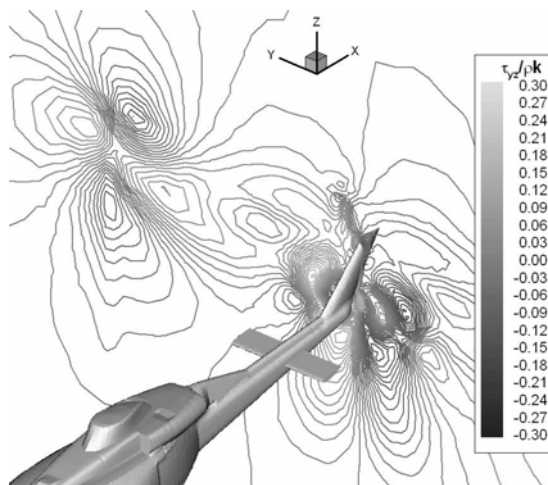


Figure 28 Normalized τ_{yz} contours at $x/L = 0.95$
 $(\alpha = -2.28$ degrees, $\psi = 0$ degrees)
 $(T = 17500$ lbs., $T_{tr} = 1104$ lbs)

Drag Predictions:

Drag predictions are performed for the cases studied above and the results are compared with the wind tunnel data²⁹, Bell simulations of Ref. 30 around their most complex configuration including the elevator and vertical tail, and LES predictions of Ref. 1. In the present work drag is computed by integrating the pressure and surface skin friction over the fuselage surface. Since the mesh was not sufficient to resolve the entire boundary layer, surface skin friction is computed using Spalding's law of the wall³¹ during the post processing. In the predictions a correction to the force in the longitudinal direction was made to take into account the faired-over inlet faces in the computation, which were open in the wind tunnel model. The dynamic head pressure was integrated over the inlet area, and subtracted from the longitudinal force component. The drag predictions in Ref. 30 contain pressure drag only while the predictions of Ref. 1 contain both pressure drag and total drag. In Ref. 1, total drag was computed by evaluating the velocity deficit in the wake of the helicopter. Table 1 shows a list of results for drag from wind tunnel measurements, Bell simulations, LES predictions and present solutions. For completeness drag predicted for the helicopter configuration with rotors is also displayed. The results showed reasonable agreement with the wind tunnel data. For the low angle of attack cruise case RSM solution predicted a drag force with a 17.6 % error which is still better than the pressure drag prediction of Ref. 30, which employed Baldwin-Lomax turbulence model, and much better than the LES predictions of Ref. 1 which uses a very coarse mesh to reduce the CPU time. A similar trend is also observed for the high angle of attack case. The present technique predicted a total drag with an error of 9.7 %. This is less than the error of the Bell simulation, which will increase once the viscous drag is added. For the high yaw angle case the total drag is underpredicted with a 14.4 % discrepancy, which is still a reasonable error considering the

differences between the wind tunnel and the computation geometries. From Table 1 one can also see that the presence of the main and tail rotors increase the pressure drag by 3 % and total drag by 2.8 %. This is an expected result because the flow condition is a high speed forward flight and the rotor wakes barely interacts with the fuselage.

CODE PERFORMANCE

Simulations are performed using an unstructured mesh of 2.9 million tetrahedral cells and required 8.77 GB of memory. Each solution took 6 days on 30 COCOA3 processors. In

Ref. 1 LES solutions performed for the same geometry took 60 days on sixteen 800 MHz Pentium III processors for a physical time of 1.25 seconds. But a much coarser mesh with 530,000 cells was used for the solutions. The present RSM solution on this coarse mesh took one day on 30 COCOA3 processors (2.4 GHz). Hence it can be concluded that RSM (3-D problem) is nearly ten times faster than LES (4-D problem).

Table 1. Drag predictions and comparison with wind tunnel data

	α (degrees)	ψ (degrees)	D/q (ft ²)	% Error
wind tunnel data (total drag) (Ref. 29)	-2.28	0	4.596	N/A
Bell Simulations (pressure drag)(Ref.30)	-2.28	0	5.466	18.9
RSM Simulation (pressure drag)	-2.28	0	4.356	5.22
RSM Simulation (total drag)	-2.28	0	5.405	17.6
LES prediction (pressure drag) (Ref. 1)	-2.28	0	4.842	5.3
LES prediction (total drag) (Ref. 1)	-2.28	0	6.225	35.4
RSM Simulation (full helicopter) (pressure drag)	-2.28	0	4.487	N/A
RSM Simulation (full helicopter) (total drag)	-2.28	0	5.547	N/A
wind tunnel data (total drag) (Ref. 29)	17.04	0	6.521	N/A
Bell Simulations (pressure drag) (Ref. 30)	17.04	0	7.163	9.8
RSM Simulation (pressure drag)	17.04	0	5.971	8.4
RSM Simulation (total drag)	17.04	0	7.159	9.7
wind tunnel data (total drag) (Ref. 29)	-1.6	16.4	15.058	N/A
RSM Simulation (pressure drag)	-1.6	16.4	11.737	22.1
RSM Simulation (total drag)	-1.6	16.4	12.886	14.4

CONCLUSIONS

High Reynolds number turbulent flow over a Bell 214ST fuselage was predicted using RSM. The model has been previously used and validated by the authors for simulation of three-dimensional separated flows. The numerical solutions were performed at a Reynolds number of 1.5×10^6 per foot and a Mach number of 0.2322. Results for flow over isolated fuselage at three flight conditions and a helicopter configuration with rotors modeled using linear momentum theory were presented. The results were also compared with wind tunnel data and other numerical simulations. Pressure correlations for low angle of attack cruise and high angle of attack conditions showed very good agreement with the experiment while some discrepancies were observed on the tail boom region for the high yaw angle case. This may be due to faired-over inlet faces which were open in the wind tunnel model. Normalized Reynolds stress contours plotted for each flow condition clearly showed the anisotropy and inhomogeneity of the current turbulent flow. The effects of flow condition on turbulence were also observed. In an attempt to see the effectiveness of RSM, a Reynolds stress (computed using Boussinesq approximation) is compared with a predicted Reynolds stress. It was concluded that Reynolds stress tensor does not align with the mean strain rate tensor and this supported the usage of a second moment closure for the predictions.

Full helicopter simulations are performed by modeling the main and the tail rotor as actuator disks. The pressure jumps across the disks are computed using momentum theory with linear loading distribution. The results are compared with the isolated fuselage results obtained for the same flow conditions. It was observed that the presence of the rotors induces additional flow gradients and tip vortices which definitely change the turbulence structure by increasing the inhomogeneity and anisotropy.

Drag predictions were performed and compared with wind tunnel data and other numerical simulations. Spalding's law of the wall is used for the surface skin friction predictions. The predictions show reasonable agreement with the wind tunnel data and RSM performed better than the Bell simulations which employed an algebraic turbulence model and LES solutions which employed a much coarser mesh to reduce the required CPU time.

Finally the performance of the present RSM is analyzed. It was concluded that RSM, which represents a three-dimensional problem, is nearly ten times faster than LES, which is a dynamic model thus represents a four-dimensional problem. RSM was also proved to be very effective in computing time averaged quantities.

ACKNOWLEDGEMENTS

This work was supported by the Army/NASA Rotorcraft Center of Excellence (RCOE) Center (NGT2-52275) at The Pennsylvania State University.

REFERENCES

1. Souliez, F. J., "Parallel Methods for Computing Unsteady Separated Flows Around Complex Geometries," Ph.D. Thesis, Penn State University, Aerospace Engineering Department, August 2002.
2. Lakshminarayana, B., "Turbulence Modeling for Complex Shear Flows," AIAA Journal, Vol.24, (12), pp 1900 – 1917, 1986
3. Wilcox, D. C., Turbulence Modeling for CFD, DCW Industries Inc, ISBN 1-928729-10-X.
4. Duque E. P. N., Dimanlig, A. C. B., "Navier-Stokes Simulation of the AH-66 (Comanche) Helicopter," AHS Aeromechanics Specialists Conference, San Francisco., CA, January 1994.
5. Duque, E.P.N., Berry, J.D., Budge, A.M., Dimanlig, A.C.B., "A Comparison of Computed and Experimental Flowfields of the RAH-66 Helicopter," AHS Aeromechanics Specialists Meeting., Connecticut, October 1995.
6. Slomski, J. F., Gorski, J. J., Miller R. W., Marioni T. A., "Numerical Simulation of Circulation Control Airfoils as Affected by Turbulence Models," AIAA 40th Aerospace Sciences Meeting & Exhibit, AIAA 2002-0851, Reno, NV, January 2002.
7. Launder, B. E., Reece, G. J., Rodi W., "Progress in the Development of a Reynolds-Stress Closure," Journal of Fluid Mechanics, vol. 68, (3), pp. 537 – 566, 1975.
8. Jindal, S., Long, L. N., Plassmann, P. E., Sezer-Uzol, N., "Large Eddy Simulations on a Sphere Using Unstructured Grids," AIAA Fluid Dynamics Conference and Exhibit, AIAA 2004-2228, Portland, OR, 2004.
9. Alpman, E., and Long, L. N., "Separated Turbulent Flow Simulations Using a Reynolds Stress Model and Unstructured Meshes," AIAA 43rd Aerospace Sciences Meeting and Exhibit, AIAA-2005-1094, January, 2005.
10. Alpman, E., "Numerical Simulation of Rotary wing Flowfields in Parallel Computers," M.S. Thesis, Aerospace Engineering Department, Middle East Technical University, Ankara, Turkey, July 2001.
11. Leishman, J. G., Principles of Helicopter Aerodynamics, Cambridge University Press, 2000, ISBN 0 521 53296 6.
12. Alpman, E., Long, L. N., and Kothmann, B. D., "Toward a Better Understanding of Ducted Rotor Antitorque and Directional Control in Forward Flight," AHS International 59th Annual Forum and Display, Phoenix, AZ, May, 2003.
13. Alpman, E., and Long, L. N., "Unsteady RAH-66 Comanche Flowfield Simulations including Fan-in-

- Fin,” AIAA 16th CFD Conference, AIAA-2003-4231, Orlando, FL, June, 2003.
14. Alpman, E., Long, L. N., and Kothmann, B. D., “Understanding Ducted Rotor Antitorque and Directional Control Characteristics, Part I: Steady State Simulation,” *Journal of Aircraft*, Vol. 41, (5), pp 1042-1053, 2004.
 15. Alpman, E., Long, L. N., and Kothmann, B. D., “Understanding Ducted Rotor Antitorque and Directional Control Characteristics, Part II: Unsteady Simulation,” *Journal of Aircraft*, Vol. 41, (6), pp 1370 – 1378, 2004.
 16. O’Brien, D. M. Jr., Smith, M. J., “Analysis of Rotor-Fuselage Interactions Using Various Rotor Models,” AIAA 43rd Aerospace Sciences Meeting and Exhibit, AIAA-2005-1094, January, 2005.
 17. Pacheco, P. S., *Parallel Programming with MPI*, Morgan Kaufmann Publishers Inc., 1997.
 18. Vandromme, D., Ha Minh H., “About Coupling of Turbulence Closure Models with Averaged Navier-Stokes Equations,” *Journal of Computational Physics*, Vol. 65, pp. 386 – 409, 1986.
 19. Daly, B. J., Harlow, F. H., “Transport Equations in Turbulence”, *Physics of Fluids*, Vol. 13 (11), pp 2634 – 2649, 1970.
 20. Gerolymos, G. A., Vallet, I., “Wall-Normal-Free Reynolds Stress Model for Rotating Flows Applied to Turbomachinery,” *AIAA Journal*, Vol. 40, (2), pp 199 – 207, 2002.
 21. Pope, S. B., *Turbulent Flows*, Cambridge University Press, ISBN 0 521 59886 9, 2000.
 22. Gerolymos, G. A., Vallet, I., “Wall-Normal-Free Reynolds Stress Closure for Three-Dimensional Compressible Separated Flows,” *AIAA Journal*, Vol. 39, (10), pp 1833 – 1842, 2001.
 23. Chassaing, J. C., Gerolymos, G. A., Vallet, “Efficient and Robust Reynolds-Stress Model Computation of Three-Dimensional Compressible Flows,” *AIAA Journal*, Vol. 41, (5), pp 763 – 773, 2003.
 24. Chassaing, J. C., Gerolymos, G. A., Vallet, “Reynolds-Stress Model Dual-Time Stepping Computation of Unsteady Three-Dimensional Flows,” *AIAA Journal*, Vol. 41, (10), pp 1882 – 1894, 2003.
 25. Launder, B. E., Shima. N., “Two-Moment Closure for the Near-Wall Sublayer: Development and Application,” *AIAA Journal*, Vol. 27, (10), pp. 1319 – 1325, 1989.
 26. Gibson, M. M., Launder B. E., “Ground Effects on Pressure Fluctuations in the Atmospheric Boundary Layer,” *Journal of Fluid Mechanics*, Vol. 86, pp. 491 – 511, 1978.
 27. Shir, C. C., “A Preliminary Numerical Study of Atmospheric Turbulent Flows in the Idealized Planetary Boundary Layer,” *Journal of Atmospheric Sciences*, Vol. 30, pp. 1327 – 1339, 1973.
 28. Roe, P. L., “Approximate Riemann Solvers, Parameter Vectors and Difference Schemes”, *Journal of Computational Physics*, Vol. 43, pp. 357 – 372, 1981.
 29. Oldenbuttel, R. H., “A Low Speed Wind Tunnel Test of Bell Helicopter Textron 0.200 Scale M214ST Model Investigating Aerodynamics Characteristics”, Report No. LSWT 554, Vought Corporation, 1978.
 30. Narramore, J. C., Brand, A.G., “Navier-Stokes Correlations to Fuselage Wind Tunnel Data,” AHS International 48th Annual Forum and Display, Washington, DC., June, 1992.
 31. Spalding, D. B., “A Single Formula for the Law of the Wall,” *Trans ASME Series A, Journal of Applied Mechanics*, Vol. 28 (3), pp. 444 – 458, 1961.